nature materials

ARTICLES

https://doi.org/10.1038/s41563-021-01082-4

The transport–structural correspondence across the nematic phase transition probed by elasto X-ray diffraction

Joshua J. Sanchez[1], Paul Malinowski[1], Joshua Mutch[1], Jian Liu[2], J.-W. Kim[3], Philip J. Ryan[3,4] and Jiun-Haw Chu[1]✉

Electronic nematicity in iron pnictide materials is coupled to both the lattice and the conducting electrons, which allows both structural and transport observables to probe nematic fluctuations and the order parameter. Here we combine simultaneous transport and X-ray diffraction measurements with in-situ tunable strain (elasto X-ray diffraction) to measure the temperature dependence of the shear modulus and elastoresistivity above the nematic transition and the spontaneous orthorhombicity and resistivity anisotropy below the nematic transition, all within a single sample of $Ba(Fe_{0.96}Co_{0.04})_2As_2$. The ratio of transport to structural quantities is nearly temperature independent over a 74 K range and agrees between the ordered and disordered phases. These results show that elasto X-ray diffraction is a powerful technique to probe the nemato-elastic and nemato-transport couplings, which have important implications to the nearby superconductivity. It also enables the measurement in the large strain limit, where the breakdown of the mean-field description reveals the intertwined nature of nematicity.

Electronic nematicity refers to a spontaneous rotational-symmetry-breaking phase in solids driven by electronic correlations[1]. It was initially discovered in a few fine-tuned systems, such as the quantum Hall states of the two-dimensional electron gas[2,3] and the field-induced metamagnetic state in $Sr_3Ru_2O_7$ (ref. [4]), but its existence was later observed in the broader class of strongly correlated systems, including iron-based[5,6] and copper-based[7,8] high-temperature superconductors and more recently in magic-angle-twisted bilayer graphene[9]. In almost all cases, the first signature of nematicity has been the onset of large resistivity anisotropy, which is regarded as a proxy of the nematic order parameter. The correspondence between the nematicity and transport anisotropy originates from symmetry considerations. The nematic order parameter ψ and the resistivity anisotropy $\eta = \frac{\rho_{xx}-\rho_{yy}}{\rho_{xx}+\rho_{yy}}$ (where ρij is the resistivity tensor) belong to the same irreducible representation of the high-symmetry point group, hence in the infinitesimal limit they are linearly proportional to each other with linear proportionality coefficient k[10] ($\eta = k\psi$). Nevertheless, the resistivity is not a thermodynamic variable and depends on extrinsic properties such as disorder[11–14]. Therefore, a key question is to what extent a transport coefficient can represent the order parameter beyond the infinitesimal limit. This question is especially important for two-dimensional systems such as graphene where thermodynamic measurements are difficult.

Here we examine this question in a model system for the study of nematic phase transitions, the iron pnictide superconductor[15,16]. Because of the electron–lattice coupling, the nematicity in iron pnictides has been clearly observed in both transport anisotropy and structural thermodynamic variables. Above the phase transition, the diverging nematic susceptibility can be seen in the Curie–Weiss temperature dependence of both the $2m_{66}$ elastoresistivity coefficient[17] and the softening of the shear modulus[18] C_{66}. Below the phase transition, the nematic order parameter also generates a large spontaneous resistivity anisotropy[6,19] η_S and a spontaneous structural distortion[20,21] ε_S. Each of these four quantities are usually measured separately due to the incompatible sample preparation needed for standard techniques, which makes a quantitative comparison difficult. In particular, the spontaneous resistivity anisotropy η_S is notoriously difficult to measure close to the phase transition, because the stress required to detwin the sample always induces additional resistivity anisotropy due to the softening of C_{66} and the divergence of $2m_{66}$. To our knowledge, no study of iron pnictides has ever reported any two of the above quantities within a single sample. In this work, we perform measurements of $2m_{66}$, C_{66}, η_S and ε_S using the technique of elasto X-ray diffraction all within one single-crystal sample of $Ba(Fe_{0.96}Co_{0.04})_2As_2$, located on the underdoped side of the phase diagram with nematic, antiferromagnetic and superconducting transition temperatures at $T_S = 73.8$ K, $T_N = 64$ K and $T_C = 13$ K, respectively (Fig. 1a). With our unprecedented multi-modal measurement, we show the four quantities perfectly follow a mean-field temperature dependence. Furthermore, the ratio of transport to structural quantities is a constant across the phase transition, suggesting that the resistivity anisotropy behaves just like a thermodynamic variable even for large values of the nematic order parameter. While the $2m_{66}$, C_{66}, η_S and ε_S can be well described by the Landau free energy framework, two unexpected findings stand out. First, using the C_{66} and $2m_{66}$ data from the previous studies[17,22], we discovered a strong doping dependence of the ratio between transport and structural quantities, increasing by more than fivefold towards optimal doping. Second, when driving the system deep into the nonlinear regime with large uniaxial stress, we found that the resistivity anisotropy shows a non-saturating behaviour that is drastically different from the dampened response of the lattice. Possible implications of these two unusual phenomena are discussed.

[1]Department of Physics, University of Washington, Seattle, WA, USA. [2]Department of Physics and Astronomy, University of Tennessee, Knoxville, TN, USA. [3]Advanced Photon Source, Argonne National Laboratories, Lemont, IL, USA. [4]School of Physical Sciences, Dublin City University, Dublin, Ireland. ✉e-mail: jhchu@uw.edu

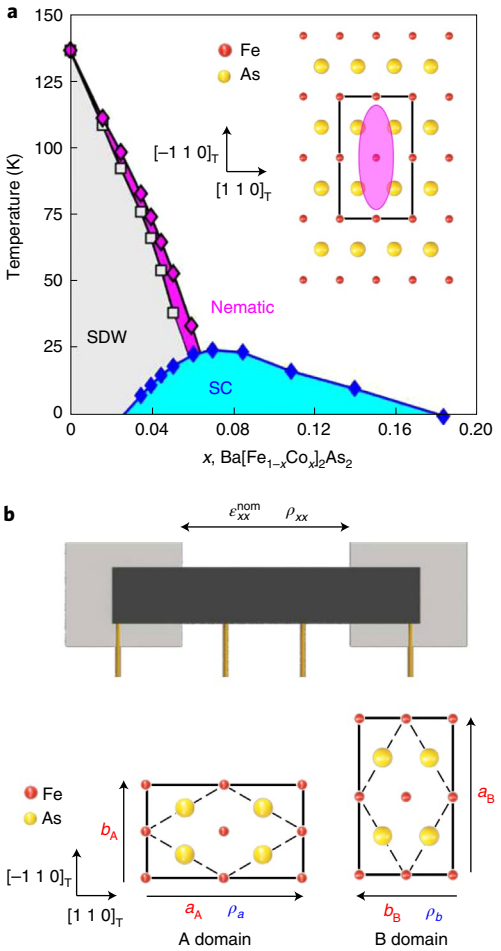

Fig. 1 | Nematic-elastic-transport coupling. a, The *x*–*T* phase diagram of Co-doped $BaFe_2As_2$. Magenta, grey and blue markers show nematic, antiferromagnetic (SDW) and superconducting (SC) transitions. Inset is a representation of the electronic nematicity (magenta, quantified by the nematic order parameter ψ) aligned with the orthorhombic lattice (black, quantified by the in-plane orthorhombicity ε). **b**, Schematic of the sample measurement geometry and strain device. Uniaxial stress is applied along the tetragonal $[110]_T$ direction. In-line resistivity ρ_{xx} measures ρ_a of the A domain and ρ_b of the B domain.

Elasto X-ray diffraction

To simultaneously assess the electronic and structural response to stress in a single-crystal sample, we have developed an experimental platform, elasto X-ray diffraction, that combines electrical transport with in-situ uniaxial stress tunability via a Razorbill CS-100 strain device[23] fully integrated with X-ray diffraction measurements at beamline 6-ID-B at the Advanced Photon Source (Fig. 1b; Methods). This platform allows us to measure the lattice constants, orthorhombic twin domain populations and electrical resistivity simultaneously while the uniaxial stress is continuously tuned to detwin the sample and enhance the orthorhombicity. At fixed temperatures from 66 K to 140 K, X-ray diffraction and transport measurements were made by ramping the strain from maximum compression to maximum tension and back. Uniaxial stress was applied along the tetragonal $[1\,1\,0]_T$ direction, which we defined as $\hat{x}$. The nominal strain is defined as $\varepsilon_{xx}^{nom} = \frac{\Delta L}{L_0}$, where L_0 is the size of the gap between two titanium plates on which the sample was glued with Stycast epoxy. The displacement ΔL was determined from a capacitance strain gauge. The four-wire electrical contact geometry enables the simultaneous resistance measurements along the stress axis.

Nematic fluctuations: shear modulus and elastoresistivity

We focus first on the structural and electronic response to applied stress above the nematic transition, where there are no orthorhombic domains. We define $\varepsilon_{xx} = \frac{\Delta a}{a_0}$ and $\varepsilon_{yy} = \frac{\Delta b}{b_0}$ as the X-ray-diffraction-measured strains of the in-line ($[1\,1\,0]_T$) and transverse ($[-1\,1\,0]_T$) lattice constants, respectively. At 130 K the lattice constants show a nearly linear response to ε_{xx}^{nom}, while just above the transition at 74 K the response becomes strongly nonlinear, with an enhanced response at $\varepsilon_{xx}^{nom} = 0$ (Fig. 2a). This results in the strain transmission $\frac{d\varepsilon_{xx}}{d\varepsilon_{xx}^{nom}}$ and the induced B_{2g} orthorhombicity $\varepsilon = \frac{1}{2}(\varepsilon_{xx} - \varepsilon_{yy})$ becoming increasingly nonlinear with cooling (Supplementary Fig. 2). The rate of change of the in-plane transverse strain to in-line strain $\frac{d\varepsilon_{yy}}{d\varepsilon_{xx}}$ approaches a peak value of −1 with cooling to T_S and decreases to its high-temperature value at large ε (Fig. 2b).

We extract the shear modulus from Poisson's ratio $\left(\nu_{xy} = -\frac{d\varepsilon_{yy}}{d\varepsilon_{xx}}|_{\varepsilon=0}\right)$ using $C_{66} = (50.5\ \text{GPa})\ \frac{1-\nu_{xy}}{1+\nu_{xy}}$, where the magnitude is determined from other elastic modulus terms using ultrasound data from the literature[22] (Supplementary Discussion Section VII). In Fig. 2c, C_{66} diminishes to nearly zero at T_S (black dots). Fitting C_{66} with a Curie–Weiss temperature dependence, $C_{66} = C_{66,0} - A(T - T^*)^{-1}$ (red line; see Methods), yields a fitted value of the bare shear modulus $C_{66,0} = 38.8 \pm 4.7$ GPa in agreement with the high-temperature ultrasound data[22]. The extracted bare nematic transition temperature, $T^* = 50 \pm 8.3$ K is considerably larger than the values obtained from several other shear modulus measurements[5,18,24,25], where $T_S - T^* \approx 40$–50 K, yet as we discuss below, it agrees well with the T^* obtained from the simultaneous elastoresistance measurement. A major difference is that in the previously reported measurements, C_{66} is reduced but non-zero at the transition, possibly due to local strain inhomogeneities and resulting domain microstructures adding a small background signal near the transition[25]. Since C_{66} varies most rapidly near the transition, this difference may strongly influence the Curie–Weiss fitting, hence the discrepancy in T^*.

We next turn to the resistivity response to strain. The resistivity ρ_{xx} versus ε_{xx}^{nom} is increasingly nonlinear with cooling (Fig. 2d). In particular, near the phase transition, ρ_{xx} shows a kink-like behaviour as ε_{xx}^{nom} increases from zero to positive, and an inflection point at large negative values of ε_{xx}^{nom}. Intriguingly, while still being nonlinear, the kink and inflection point of ρ_{xx} vanish when plotted against the simultaneously measured orthorhombicity ε (Fig. 2e), and ρ_{xx} can be well fitted by a second-order polynomial (Supplementary Fig. 3). This stark contrast indicates that the anomalies observed in ρ_{xx} versus ε_{xx}^{nom} are artefacts of the nonlinear strain transmission, highlighting the importance of in-situ X-ray measurements. The second-order polynomial can be understood from a symmetry analysis by decomposing the in-line resistivity dependence on the B_{2g} orthorhombicity as

$\rho_{xx}(\varepsilon) = \rho_0\left(1 + m_{B_{2g}}^{B_{2g}}\varepsilon + m_{A_{1g}}^{B_{2g},B_{2g}}\varepsilon^2\right)$, where ρ_0 is the zero-stress resistivity, $m_{B_{2g}}^{B_{2g}} = 2m_{66}$ is the linear coefficient with (odd) B_{2g} symmetry and $m_{A_{1g}}^{B_{2g},B_{2g}}$ is the quadratic coefficient with (even) A_{1g} symmetry. Consistent with previous work[26], $m_{A_{1g}}^{B_{2g},B_{2g}}$ has a large magnitude near the transition. As we cannot perform a simultaneous bidirectional transport measurement with this set-up, we isolate the B_{2g} component and extract the $2m_{66}$ elastoresistivity coefficient at each temperature using $2m_{66} = \frac{d}{d\varepsilon}\left(\frac{\Delta\rho_{xx}}{\rho_0}\right)|_{\varepsilon=0}$, which diverges towards the transition (Fig. 2f). We analyse this temperature dependence with the same Curie–Weiss model as that used for the shear modulus and find it is well described with a similar $T^* = 48.9 \pm 7.1$ K (Fig. 3e, blue line, $R^2 > 0.95$). Therefore, we demonstrate that

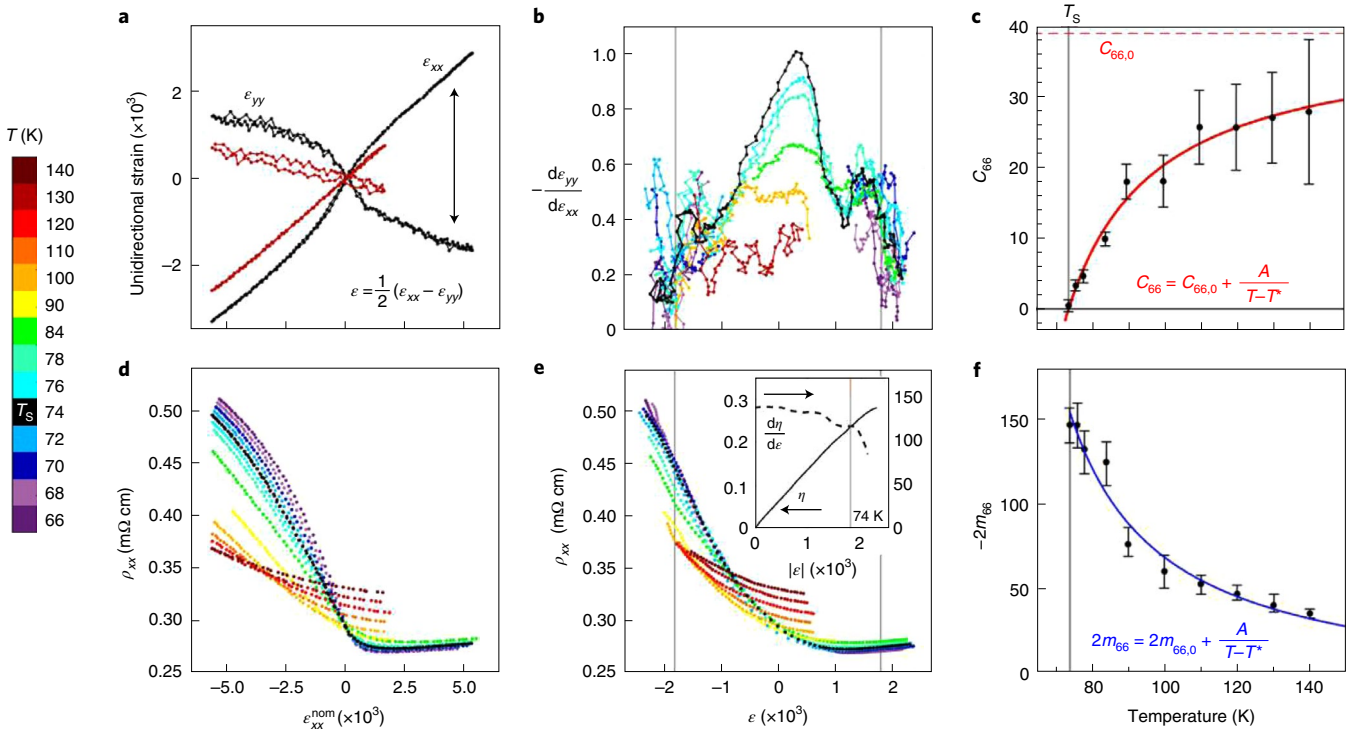

Fig. 2 | Shear modulus and elastoresistivity. a, Unidirectional lattice constant strains ε_{xx} and ε_{yy} versus nominal strain ε_{xx}^{nom} at $T = 74$ K (black) and 130 K (red). In-plane orthorhombicity $\varepsilon = \frac{1}{2}(\varepsilon_{xx} - \varepsilon_{yy})$. **b**, The rate of change of in-plane unidirectional strains $-\frac{d\varepsilon_{yy}}{d\varepsilon_{xx}}$ versus ε. **c**, The shear modulus C_{66} extracted from $\nu_{xy} = -\frac{d\varepsilon_{yy}}{d\varepsilon_{xx}}|_{\varepsilon=0}$; error bars are the standard deviation of a small strain range linear regression (Supplementary Discussion Section VI). **d**,**e**, Longitudinal resistivity ρ_{xx} versus ε_{xx}^{nom} (**d**) and ρ_{xx} versus ε (**e**). Inset to **e** shows the resistivity anisotropy $\eta = \frac{\rho_{xx}(\varepsilon)-\rho_{xx}(-\varepsilon)}{\rho_{xx}(\varepsilon)+\rho_{xx}(-\varepsilon)}$ and the derivative $\frac{d\eta}{d\varepsilon}$ at $T = 74$ K. **f**, The $2m_{66}$ elastoresistivity extracted from $\frac{d\rho/\rho_0}{d\varepsilon}|_{\varepsilon=0}$; lower/upper error bars show the value of $\frac{d\rho/\rho_0}{d\varepsilon}$ determined at $\varepsilon = \pm 0.01\%$. Fit lines in **c** and **f** are described in the main text. Grey lines in **b** and **e** show the 8 K zero-stress value of in-plane orthorhombicity, $\varepsilon = 0.18\%$.

both $2m_{66}$ and C_{66} within a single sample show the same mean-field temperature dependence, confirming that both have a linear proportionality to a common driver, namely the nematic fluctuations.

While the $2m_{66}$ and C_{66} extracted near the zero-strain limit show good agreement with mean-field behaviour, that is no longer the case in the large strain limit where nematic fluctuations are expected to be heavily dampened. The Fig. 2e inset shows the resistivity anisotropy $\eta = \frac{\rho_{xx}(\varepsilon)-\rho_{xx}(-\varepsilon)}{\rho_{xx}(\varepsilon)+\rho_{xx}(-\varepsilon)}$, defined as the normalized resistivity difference at equal in-plane orthorhombicity between tension and compression, and its strain derivative $\frac{d\eta}{d\varepsilon}$, which corresponds to the induced nematic order parameter and nematic susceptibility at finite strain (note that $\frac{d\eta}{d\varepsilon}|_{\varepsilon=0} = \frac{d}{d\varepsilon}\left(\frac{\Delta\rho_{xx}}{\rho_0}\right)|_{\varepsilon=0} = 2m_{66}$). At temperatures near or below T_S, η shows no sign of saturation as ε exceeds 0.18% (the spontaneous orthorhombicity at $T = 8$ K, which is also the maximum value of spontaneous orthorhombicity for this doping concentration). This non-saturating behaviour is in sharp contrast to the structural counterpart, where $\frac{d\varepsilon_{yy}}{d\varepsilon_{xx}}$ dampens rapidly towards its high temperature value (Fig. 2b). Although in the large-stress limit, $\frac{d\varepsilon_{yy}}{d\varepsilon_{xx}}$ and $\frac{d\eta}{d\varepsilon}$ no longer simply relate to C_{66} and $2m_{66}$, which are response functions defined in the zero-stress limit, the striking difference between $\frac{d\varepsilon_{yy}}{d\varepsilon_{xx}}$ and $\frac{d\eta}{d\varepsilon}$ is unexpected. This peculiar finding will be revisited in the Discussion section.

Spontaneous elastoresistivity

Next, we extract the spontaneous orthorhombicity ε_S and spontaneous resistivity anisotropy η_S in the nematic ordered phase. We focus on the 10 K range below T_S but above T_N because the long-range antiferromagnetic order induces shifts in the orthorhombicity[20,21] and reconstructs the Fermi surface leading to additional resistivity anisotropy effects[27–30]. Upon cooling the sample below $T_S = 73.8$ K, the single peak of the $(2\,2\,12)_T$ reflection splits into two peaks corresponding to the a_A and b_B orthorhombic lattice constants of the A and B domains, respectively, indicating the formation of structural twin domains (Fig. 3a). As is often done for a free-standing crystal[21], we define the spontaneous orthorhombicity as $\varepsilon_S = \frac{a_A - b_B}{a_A + b_B}$ in the zero-stress limit. Within the purely nematic phase, ε_S is well fitted to a mean-field $\sqrt{T_S - T}$ temperature dependence (Fig. 3f).

The presence of twin domains causes transport measurements to average over the resistivities along the two domain directions. This presents a substantial experimental challenge to obtaining the resistivity anisotropy of the orthorhombic unit cell, which we overcome by precisely strain detwinning the sample. Figure 3c–e shows detwinning results for a representative temperature (66 K). The peak positions and intensities (I_A and I_B) are shown in Fig. 3c. Strain homogeneity is confirmed by a nearly constant Bragg peak width throughout the nominal strain range (Fig. 3d). The relative volume fraction of the A domain is determined as $D_A = \left(\frac{I_A}{I_A + I_B}\right) \times 100\%$, which varies smoothly between 0% and 100% with applied stress, that is, between the B and A monodomains (Fig. 3e, right). While the sample is mostly detwinned over a relatively small strain range, the last ~10% volume fraction of the minor domain is detwinned over larger strain values where the in-line lattice constant becomes highly susceptible to applied strain. Therefore, we find that we can mostly, but not fully, detwin the sample without inducing additional lattice distortions, which warrants consideration for the design and interpretation of future experiments involving the uniaxial stress detwinning of structural domains.

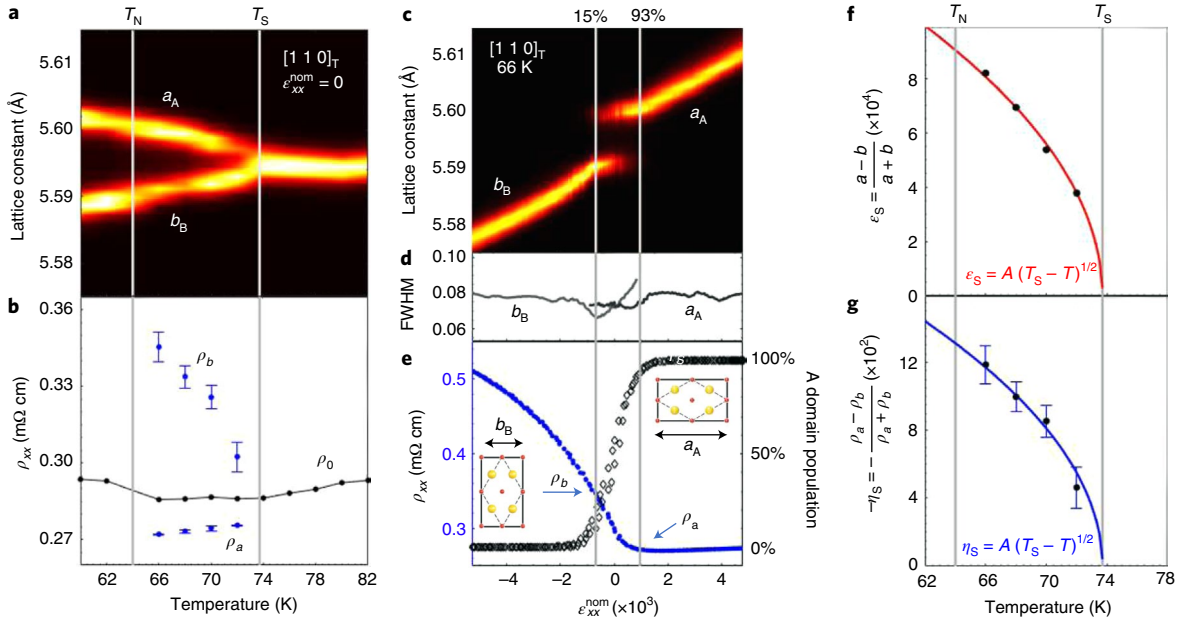

Fig. 3 | Spontaneous resistivity anisotropy and orthorhombicity. a, Zero-stress X-ray diffraction of the $[110]_T$ lattice constants across the nematic (T_S) and antiferromagnetic (T_N) transitions. **b**, The zero-stress twinned state resistivity $\rho_{xx,0}$ (black) and the detwinned monodomain resistivities ρ_a and ρ_b (blue) extracted from $D_A = 93\%$ and 15% points, respectively (**e** for more information). Upper and lower error bars show the value of ρ_{xx} measured during the tensioning half and compressing half, respectively, of the strain loop, while marker shows the averaged value. **c**, X-ray diffraction of the $[110]_T$ lattice constants a_A and b_B with intensities I_A and I_B. **d**, The full-width half maximum (FWHM) of the Gaussian fit to the X-ray diffraction peak for both a_A and b_B. **e**, Right axis: relative A domain population, $D_A = \frac{I_A}{I_A + I_B}$. Grey bars at $D_A = 15\%$ and $D_A = 93\%$. Left axis: in-line resistivity with monodomain resistivities ρ_a and ρ_b at $D_A = 93\%$ and $D_A = 15\%$. Inset shows orientation of detwinned monodomain and corresponding XRD-measured lattice constant in each strain limit. **f**,**g**, The spontaneous orthorhombicity ε_S (**f**) and the spontaneous resistivity anisotropy η_S (**g**) are both well fitted to a $\sqrt{T_S - T}$ temperature dependence within the nematic phase with $T_S = 73.8$ K. Error bars in **f** are from error propagation of uncertainties of ρ_a and ρ_b in **b**.

The spontaneous resistivity anisotropy $\eta_S = \frac{\rho_a - \rho_b}{\rho_a + \rho_b}$ results from the different resistivities along the a and b orthorhombic lattice vector directions, ρ_a and ρ_b. Due to the network of twin domains running at 45° to the length of the sample[31], the current takes non-trivial paths, which results in a nonlinear dependence of ρ_{xx} on D_A (Supplementary Fig. 7a). We approach the problem from two directions. First, we start in a zero nominal strain state and detwin the sample just until the lattice begins to deform (at 85% and 93% full detwinning to the compressive B and tensile A domains, respectively; Supplementary Fig. 6). This is the closest condition to a single domain state without lattice distortion that we can achieve experimentally. The extracted ρ_a and ρ_b (Fig. 3b) yield values of η_S that are well fit to $\sqrt{T_S - T}$ (Fig. 3g). Alternatively, we can extract η_S by starting in the fully detwinned regime and linearly fitting the resistivity anisotropy η down to ε_S. The resulting values of η_S are also well fit by $\sqrt{T_S - T}$ (Supplementary Fig. 7bd). The η_S values obtained by these two approaches agree within 5%, suggesting that the remnant minor domain has a minimal impact on the transport. This result stands in sharp contrast to earlier works using fixed-strain/stress detwinning in a clamp or horseshoe device[6,11,19,32–35], which generally found a large resistivity anisotropy above T_S from the strain-induced $2m_{66}$ that mixes with the detwinned domain η_S below T_S, preventing a determination of the real mean-field development of η_S. Thus, our elasto X-ray diffraction technique allows for a precise measurement of the spontaneous elastoresistivity transport coefficient, defined as a resistivity anisotropy η_S and structural order parameter ε_S driven by the system itself in the zero-stress limit. In the next section, we describe the physical interpretation of the spontaneous elastoresistivity and how it is related to $2m_{66}$ and C_{66} above the transition.

Transport–structural proportionality

The shared mean-field temperature dependence of η_S and ε_S below the transition echo the shared Curie–Weiss temperature dependence of the $2m_{66}$ and C_{66} above the transition, demonstrating the one-to-one correspondence between the transport and structural coefficients. The remaining question is whether this one-to-one correspondence is continuous across the phase transition. In Fig. 4b we plot the spontaneous elastoresistivity $\frac{\eta_S}{\varepsilon_S}$ and $2m_{66}\left(1 - \frac{C_{66}}{C_{66,0}}\right)^{-1}$. These two quantities are the ratios between the dimensionless transport and structural coefficients below and above T_S, respectively. We find that both quantities show almost no temperature dependence, and their temperature-averaged values are in strong agreement, with $\frac{\eta_S}{\varepsilon_S} = 142.6 \pm 20.7$ and $2m_{66}\left(1 - \frac{C_{66}}{C_{66,0}}\right)^{-1} = 142.9 \pm 29.7$. This agreement suggests that for the entire temperature range of this study, the resistivity anisotropy behaves like a thermodynamic order parameter for all practical purposes. We note that this relationship is valid even at the lowest measured temperature within the pure nematic phase, 66 K, where the orthorhombicity reaches ~40% of its saturation value at base temperature, well beyond the infinitesimal limit.

We now show that $\frac{\eta_S}{\varepsilon_S}$ and $2m_{66}\left(1 - \frac{C_{66}}{C_{66,0}}\right)^{-1}$ can be taken as the relative coupling of nematicity to the conducting electrons compared to the lattice. We consider the Landau free energy that describes a nematic phase transition with a bilinear coupling to the lattice (full derivation in Methods):

$$F = \frac{a(T - T^*)}{2}\psi^2 + \frac{b}{4}\psi^4 + \frac{C_{66,0}}{2}\varepsilon^2 - \lambda\psi\varepsilon$$

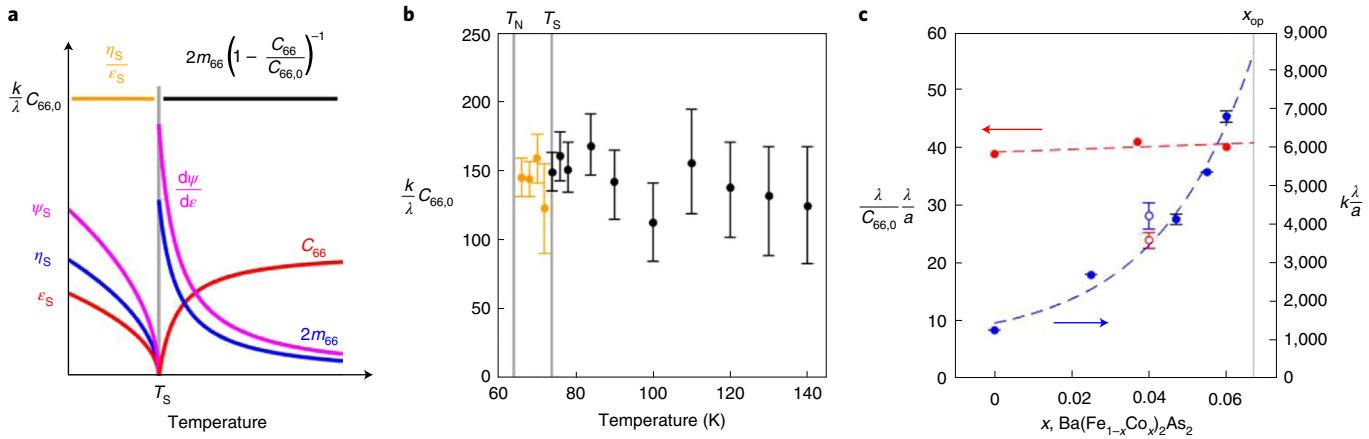

Fig. 4 | Transport–structural ratio equivalence. a, For $T < T_s$, the spontaneous nematic order parameter $\psi_S \propto \sqrt{T_S - T}$ drives the linear proportional spontaneous orthorhombicity $\varepsilon_S = \frac{\lambda}{C_{66,0}}\psi_S$ and spontaneous resistivity anisotropy $\eta_S = k\psi_S$, yielding a temperature-independent ratio $\frac{\eta_S}{\varepsilon_S}$. For $T > T_S$ the diverging nematic susceptibility $\frac{d\psi}{d\epsilon} = \frac{\lambda}{a(T^*-T)}$ drives the diverging elastoresistivity $2m_{66} = k\frac{d\psi}{d\epsilon}$ and the softened shear modulus $C_{66} = C_{66,0} - \lambda\frac{d\psi}{d\epsilon}$. The ratio $2m_{66}\left(1 - \frac{C_{66}}{C_{66,0}}\right)^{-1}$ is thus also temperature independent. If the nematic-elastic (λ) and nematic-transport (k) proportionality coefficients are constant across the phase transition, both ratios equate at T_S with a value $\frac{k}{\lambda}C_{66,0}$. **b**, The measured ratios $\frac{\eta_S}{\varepsilon_S}$ (gold) and $2m_{66}\left(1 - \frac{C_{66}}{C_{66,0}}\right)^{-1}$ (black) versus temperature (error bars are from error propagation of each quantity). **c**, The Curie constants from Curie–Weiss fits to $2m_{66}$ (blue) and C_{66} (red) across the underdoped side of the phase diagram. Data from refs. [17,22] (in main text). Dashed lines are a guide to the eye, and solid vertical line is at optimal Co doping $x_{op} = 0.067 \pm 0.02$. Open symbols are from this work. Error bars are from standard deviation of the fit.

where λ is the nemato-elastic coupling constant. Minimizing the free energy below the phase transition, we obtain the primary nematic order parameter $\psi_S \propto \sqrt{T_S - T}$ which induces a secondary order parameter, the spontaneous orthorhombicity $\varepsilon_S = \frac{\lambda}{C_{66,0}}\psi_S$. Combined with the linear nemato-transport relation $\eta_S = k\psi_S$, we get $\frac{\eta_S}{\varepsilon_S} = \frac{k}{\lambda}C_{66,0}$. Minimizing the free energy above the phase transition yields a Curie–Weiss nematic susceptibility $\frac{d\psi}{d\epsilon} = \frac{\lambda}{a(T-T^*)}$, which results in $2m_{66} = k\frac{\lambda}{a(T-T^*)}$ and $\frac{C_{66}}{C_{66,0}} = 1 - \frac{\lambda}{C_{66,0}}\frac{\lambda}{a(T-T^*)}$. From this we find $2m_{66}\left(1 - \frac{C_{66}}{C_{66,0}}\right)^{-1} = \frac{k}{\lambda}C_{66,0}$, identical to $\frac{\eta_S}{\varepsilon_S}$ below the transition (Fig. 4a). If we ignore $C_{66,0}$, which is a material specific parameter not related to nematicity, we have a simple physical interpretation of $\frac{\eta_S}{\varepsilon_S}$ and $2m_{66}\left(1 - \frac{C_{66}}{C_{66,0}}\right)^{-1}$; they measure the ratio of the nemato-transport coupling constant k and nemato-elastic coupling constant λ.

Discussion

Extensive measurements of $2m_{66}$ and C_{66} have been made across the phase diagram of Ba(Fe$_{1-x}$Co$_x$)$_2$As$_2$. In Fig. 4c we plot the fitted Curie constant $\left(k\frac{\lambda}{a}\right)$ for the $2m_{66}$ data from ref. [17] and $\left(\frac{\lambda}{C_{66,0}}\frac{\lambda}{a}\right)$ for the C_{66} data from the literature[24], which demonstrates that while $\left(k\frac{\lambda}{a}\right)$ is enhanced towards the optimal doping, $\left(\frac{\lambda}{C_{66,0}}\frac{\lambda}{a}\right)$ is not similarly enhanced. This observation suggests that the enhancement of $2m_{66}$ with doping is due not only to an enhancement of nematic fluctuations themselves but also due to a relative enhancement of nematic coupling to conduction electrons over the lattice. Indeed, we find that $2m_{66}\left(1 - \frac{C_{66}}{C_{66,0}}\right)^{-1}$, or $\frac{k}{\lambda}C_{66,0}$, increases by more than a factor of five towards the optimal doping. Given that $C_{66,0}$ shows only weak doping dependence[22], the increase of $\frac{k}{\lambda}C_{66,0}$ can only come from the relative increase of k over λ, a condition that favours the superconducting pairing by nematic fluctuations[36]. A similar conclusion was made in a recent work comparing the doping evolution of the elastocaloric effect and elastoresistivity in this same system[37], which found evidence for a diminishing value of λ with doping towards optimal. Further, elastoresistivity measurements have shown a similar increase of $k\frac{\lambda}{a}$ near quantum critical points across systems as diverse as La(Fe$_{1-x}$Co$_x$)AsO and FeSe$_{1-x}$S$_x$, suggesting that this enhancement of nematic-transport coupling near the quantum critical point may be quite general in the iron-based superconductors[38,39] (Supplementary Fig. 10).

The efficacy of resistivity anisotropy as a representation of a thermodynamic order parameter and its breakdown in the large-stress limit has a profound implication to the microscopic mechanism of nematicity. In the framework of Boltzmann transport theory, resistivity anisotropy is determined by the anisotropy of elastic and inelastic scattering rates and Fermi surfaces. Several theoretical studies have argued that anisotropic spin fluctuations, the leading candidate of the microscopic mechanism of nematicity in iron pnictides, generate anisotropy in both elastic and inelastic scattering[12,13,40]. This picture provides a natural explanation for the non-saturating resistivity anisotropy in the large-stress limit. The large stress shifts the antiferromagnetic transition to a higher temperature, which increases the spin fluctuations[41] and hence induces additional resistivity anisotropy. This is a nonlinear effect that arises from the intertwined nature of vestigial nematicity[42], which is not captured in the Landau free energy discussed above. We note that this highly nonlinear nemato-elastic coupling has also been observed in a recent elasto scanning tunnelling microscopy measurement[43]. Further, a recent study of FeSe shows a similar breakdown of transport–structural correspondence as the order parameter grows beyond 50%, which may be related to the unusual spin fluctuations in this system[44]. Future study using elasto X-ray diffraction on multiple material systems will help clarify this issue.

From the experimental perspective, the use of X-ray diffraction gives unprecedented detail in the detwinning process itself and reveals highly nonlinear structural and electronic responses close to the phase transition. While similar uniaxial stress approaches have been used recently to explore interesting properties in iron pnictides and beyond[41,45–52], this work highlights the importance

of in-situ microscopic measurement of structurally complex quantum materials.

Online content

Any methods, additional references, Nature Research reporting summaries, source data, extended data, supplementary information, acknowledgements, peer review information; details of author contributions and competing interests; and statements of data and code availability are available at https://doi.org/10.1038/s41563-021-01082-4.

Received: 29 June 2020; Accepted: 15 July 2021;
Published online: 26 August 2021

References

1. Fradkin, E., Kivelson, S. A., Lawler, M. J., Eisenstein, J. P. & Mackenzie, A. P. Nematic Fermi fluids in condensed matter physics. *Annu. Rev. Condens. Matter Phys.* **1**, 153–178 (2010).
2. Lilly, M. P., Cooper, K. B., Eisenstein, J. P., Pfeiffer, L. N. & West, K. W. Evidence for an anisotropic state of two-dimensional electrons in high Landau levels. *Phys. Rev. Lett.* **82**, 394–397 (1999).
3. Du, R. R. et al. Strongly anisotropic transport in higher two-dimensional Landau levels. *Solid State Commun.* **109**, 389–394 (1999).
4. Borzi, R. A. et al. Formation of a nematic fluid at high fields in $Sr_3Ru_2O_7$. *Science* **315**, 214–217 (2007).
5. Fernandes, R. M. et al. Effects of nematic fluctuations on the elastic properties of iron arsenide superconductors. *Phys. Rev. Lett.* **105**, 157003 (2010).
6. Chu, J.-H. et al. In-plane resistivity anisotropy in an underdoped iron arsenide superconductor. *Science* **329**, 824–826 (2010).
7. Hinkov, V. et al. Electronic liquid crystal state in the high-temperature superconductor $YBa_2Cu_3O_{6.45}$. *Science* **319**, 597–600 (2008).
8. Ando, Y., Segawa, K., Komiya, S. & Lavrov, A. N. Electrical resistivity anisotropy from self-organized one dimensionality in high-temperature superconductors. *Phys. Rev. Lett.* **88**, 137005 (2002).
9. Cao, Y. et al. Nematicity and competing orders in superconducting magic-angle graphene. *Science* **372**, 264–271 (2021).
10. Shapiro, M. C., Hristov, A. T., Palmstrom, J. C., Chu, J. & Fisher, I. R. Measurement of the B_{1g} and B_{2g} components of the elastoresistivity tensor for tetragonal materials via transverse resistivity configurations. *Rev. Sci. Instrum.* **87**, 063902 (2016).
11. Ishida, S. et al. Anisotropy of the in-plane resistivity of underdoped $Ba(Fe_{1-x}Co_x)_2As_2$ superconductors induced by impurity scattering in the antiferromagnetic orthorhombic phase. *Phys. Rev. Lett.* **110**, 207001 (2013).
12. Gastiasoro, M. N., Paul, I., Wang, Y., Hirschfeld, P. J. & Andersen, B. M. Emergent defect states as a source of resistivity anisotropy in the nematic phase of iron pnictides. *Phys. Rev. Lett.* **113**, 127001 (2014).
13. Fernandes, R. M., Abrahams, E. & Schmalian, J. Anisotropic in-plane resistivity in the nematic phase of the iron pnictides. *Phys. Rev. Lett.* **107**, 217002 (2011).
14. Kuo, H. H. & Fisher, I. R. Effect of disorder on the resistivity anisotropy near the electronic nematic phase transition in pure and electron-doped $BaFe_2As_2$. *Phys. Rev. Lett.* **112**, 227001 (2014).
15. Lederer, S., Schattner, Y., Berg, E. & Kivelson, S. A. Enhancement of superconductivity near a nematic quantum critical point. *Phys. Rev. Lett.* **114**, 097001 (2015).
16. Chen, X., Maiti, S., Fernandes, R. M. & Hirschfeld, P. J. Nematicity and superconductivity: competition versus cooperation. *Phys. Rev. B* **102**, 184512 (2020).
17. Kuo, H. H., Chu, J. H., Palmstrom, J. C., Kivelson, S. A. & Fisher, I. R. Ubiquitous signatures of nematic quantum criticality in optimally doped Fe-based superconductors. *Science* **352**, 958–962 (2016).
18. Yoshizawa, M. et al. Structural quantum criticality and superconductivity in iron-based superconductor $Ba(Fe_{1-x}Co_x)_2As_2$. *J. Phys. Soc. Jpn* **81**, 024604 (2012).
19. Tanatar, M. A. et al. Uniaxial-strain mechanical detwinning of $CaFe_2As_2$ and $BaFe_2As_2$ crystals: optical and transport study. *Phys. Rev. B* **81**, 184508 (2010).
20. Nandi, S. et al. Anomalous suppression of the orthorhombic lattice distortion in superconducting $Ba(Fe_{1-x}Co_x)_2As_2$ single crystals. *Phys. Rev. Lett.* **104**, 057006 (2010).
21. Kim, M. G. et al. Character of the structural and magnetic phase transitions in the parent and electron-doped $BaFe_2As_2$ compounds. *Phys. Rev. B* **83**, 134522 (2011).
22. Fujii, C. et al. Anisotropic Grüneisen parameter and diverse order parameter fluctuations in iron-based superconductor $Ba(Fe_{1-x}Co_x)_2As_2$. *J. Phys. Soc. Jpn* **87**, 074710 (2018).
23. Hicks, C. W., Barber, M. E., Edkins, S. D., Brodsky, D. O. & Mackenzie, A. P. Piezoelectric-based apparatus for strain tuning. *Rev. Sci. Instrum.* **85**, 065003 (2014).
24. Böhmer, A. E. et al. Nematic susceptibility of hole-doped and electron-doped $BaFe_2As_2$ iron-based superconductors from shear modulus measurements. *Phys. Rev. Lett.* **112**, 047001 (2014).
25. Carpenter, M. et al. Ferroelasticity, anelasticity and magnetoelastic relaxation in Co-doped iron pnictide: $Ba(Fe_{0.957}Co_{0.043})_2As_2$. *J. Phys. Condens. Matter* **31**, 155401 (2019).
26. Palmstrom, J. C., Hristov, A. T., Kivelson, S. A., Chu, J. H. & Fisher, I. R. Critical divergence of the symmetric (A_{1g}) nonlinear elastoresistance near the nematic transition in an iron-based superconductor. *Phys. Rev. B* **96**, 205133 (2017).
27. Analytis, J. G. et al. Quantum oscillations in the parent pnictide $BaFe_2As_2$: itinerant electrons in the reconstructed state. *Phys. Rev. B* **80**, 064507 (2009).
28. Shimojima, T. et al. Orbital-dependent modifications of electronic structure across the magnetostructural transition in $BaFe_2As_2$. *Phys. Rev. Lett.* **104**, 057002 (2010).
29. Nakajima, M. et al. Unprecedented anisotropic metallic state in undoped iron arsenide $BaFe_2As_2$ revealed by optical spectroscopy. *Proc. Natl Acad. Sci. USA* **108**, 12238–12242 (2011).
30. Watson, M. D. et al. Probing the reconstructed Fermi surface of antiferromagnetic $BaFe_2As_2$ in one domain. *npj Quantum Mater.* **4**, 36 (2019).
31. Tanatar, M. A. et al. Direct imaging of the structural domains in the iron pnictides AFe_2As_2 (A = Ca,Sr,Ba). *Phys. Rev. B* **79**, 180508(R) (2009).
32. Tanatar, M. A. et al. Origin of the resistivity anisotropy in the nematic phase of FeSe. *Phys. Rev. Lett.* **117**, 127001 (2016).
33. Liu, L. et al. In-plane electronic anisotropy in the antiferromagnetic orthorhombic phase of isovalent-substituted $Ba(Fe_{1-x}Ru_x)_2As_2$. *Phys. Rev. B* **92**, 094503 (2015).
34. Blomberg, E. C. et al. In-plane anisotropy of electrical resistivity in strain-detwinned $SrFe_2As_2$. *Phys. Rev. B* **83**, 134505 (2011).
35. Fisher, I. R., Degiorgi, L. & Shen, Z. X. In-plane electronic anisotropy of underdoped '122' Fe-arsenide superconductors revealed by measurements of detwinned single crystals. *Rep. Prog. Phys.* **74**, 124506 (2011).
36. Paul, I. & Garst, M. Lattice effects on nematic quantum criticality in metals. *Phys. Rev. Lett.* **118**, 227601 (2017).
37. Ikeda, M. S. et al. Elastocaloric signature of nematic fluctuations. Preprint at https://arxiv.org/abs/2101.00080 (2020).
38. Hong, X. et al. Evolution of the nematic susceptibility in $LaFe_{1-x}Co_xAsO$. *Phys. Rev. Lett.* **125**, 067001 (2020).
39. Hosoi, S. et al. Nematic quantum critical point without magnetism in $FeSe_{1-x}S_x$ superconductors. *Proc. Natl Acad. Sci. USA* **113**, 8139–8143 (2016).
40. Breitkreiz, M., Brydon, P. M. R. & Timm, C. Resistive anisotropy due to spin-fluctuation scattering in the nematic phase of iron pnictides. *Phys. Rev. B* **90**, 121104 (2014).
41. Kissikov, T. et al. Uniaxial strain control of spin-polarization in multicomponent nematic order of $BaFe_2As_2$. *Nat. Commun.* **9**, 1058 (2018).
42. Fernandes, R. M., Orth, P. P. & Schmalian, J. Intertwined vestigial order in quantum materials: nematicity and beyond. *Annu. Rev. Condens. Matter Phys.* **10**, 133–154 (2019).
43. Andrade, E. F. et al. Visualizing the nonlinear coupling between strain and electronic nematicity in the iron pnictides by elasto-scanning tunneling spectroscopy. Preprint at https://arxiv.org/abs/1812.05287 (2018).
44. Bartlett, J. et al. Relationship between transport anisotropy and nematicity in FeSe. *Phys. Rev. X* **33**, 021038 (2021).
45. Schmidt, J. et al. Nematicity in the superconducting mixed state of strain detwinned underdoped $Ba(Fe_{1-x}Co_x)_2As_2$. *Phys. Rev. B* **99**, 064515 (2019).
46. Pfau, H. et al. Detailed band structure of twinned and detwinned $BaFe_2As_2$ studied with angle-resolved photoemission spectroscopy. *Phys. Rev. B* **99**, 035118 (2019).
47. Zheng, X. Y., Feng, R., Ellis, D. S. & Kim, Y. J. Bulk-sensitive imaging of twin domains in $La_{2-x}Sr_xCuO_4$ under uniaxial pressure. *Appl. Phys. Lett.* **113**, 071906 (2018).
48. Kim, H. H. et al. Uniaxial pressure control of competing orders in a high-temperature superconductor. *Science* **362**, 1040–1044 (2018).
49. Ikeda, M. S. et al. Symmetric and antisymmetric strain as continuous tuning parameters for electronic nematic order. *Phys. Rev. B* **98**, 245133 (2018).
50. Dhital, C. et al. Effect of uniaxial strain on the structural and magnetic phase transitions in $BaFe_2As_2$. *Phys. Rev. Lett.* **108**, 087001 (2012).
51. Lu, X. et al. Nematic spin correlations in the tetragonal state of uniaxial-strained $BaFe_{2-x}Ni_xAs_2$. *Science* **345**, 657–660 (2014).
52. Malinowski, P. et al. Suppression of superconductivity by anisotropic strain near a nematic quantum critical point. *Nat. Phys.* https://doi.org/10.1038/s41567-020-0983-9 (2020).

Methods

Sample preparation. Single-crystal samples of $Ba(Fe_{0.96}Co_{0.04})_2As_2$ were grown from an FeAs flux as described elsewhere[17]. The primary sample used in X-ray measurements was prepared as a thin bar of dimensions 2.0 mm × 0.57 mm × 0.07 mm and cut along the Fe–Fe bonding direction. Gold wires were glued with DuPont 4929 silver epoxy underneath the sample to not obstruct the X-ray diffraction off the top surface of the crystal. Measurements of the resistivity coefficient ρ_{xx} aligned along the stress axis were performed using a standard four-point measurement and an SR830 lock-in amplifier.

X-ray diffraction. X-ray diffraction measurements were performed at the Advanced Photon Source, beamline 6-ID-B, at Argonne National Laboratories. X-rays of energy 11.215 keV illuminated an area 500 µm × 500 µm, fully encompassing a cross section of the middle of the crystal where strain transmission is highest. The sample and strain device were mounted on a closed-cycle cryostat. Gaussian fits to the tetragonal $(2\,2\,12)_T$, $(-1\,1\,14)_T$ and $(0\,0\,14)_T$ reflections were used to determine the orthorhombic lattice constants in the direction of applied stress (a_A and b_B), in-plane transverse to the stress (a_B and b_A) and normal to the plane (c), corresponding to the $\hat{x}$, $\hat{y}$ and $\hat{z}$ directions, respectively.

Fitting parameters. Below are the fitting parameters used in Figs. 2c, 2f, 3f and 3g, respectively:

$C_{66} = C_{66,0} + \left(\frac{A}{T-T^*}\right)$; $T^* = 50.0 \pm 8.3$ K, $A = -933 \pm 51$ GPa K, $C_{66,0} = 38.8 \pm 4.7$ GPa, $R^2 = 0.98$.

$2m_{66} = 2m_{66,0} + \left(\frac{A}{T-T^*}\right)$; $T^* = 48.9 \pm 7.1$ K, $A = -4{,}237 \pm 330$ K, $2m_{66,0} = -14.3 \pm 8.5$, $R^2 = 0.95$.

$\varepsilon_S = A\sqrt{73.8\text{ K} - T}$, $A = 0.000290 \pm 0.0000006$ K$^{-1/2}$, $R^2 = 0.99$.

$\eta_S = A\sqrt{73.8\text{ K} - T}$, $A = 0.0421 \pm 0.0022$ K$^{-1/2}$, $R^2 = 0.97$.

The $2m_{66}$ data from ref. [17] for 4.7% Co doping were reevaluated to yield fit values:

$2m_{66} = 2m_{66,0} + \left(\frac{A}{T-T^*}\right)$; $T^* = 36.4\text{ K} \pm 0.9$ K, $A = -4{,}150 \pm 135$, $2m_{66,0} = -23.1 \pm 1.0$, $R^2 = 0.99$.

Domain detwinning video. A video of the detwinning process is available online. At 66 K, strain is applied through a loop from maximum compression to maximum tension and back. In the video, the top plot shows the log-scale intensity of the split $(2\,2\,12)_T$ peak across the whole area detector ('chi' versus 2θ). The shifts in intensity across the 'chi' direction (y axis) indicate small reorientations of crystal grains, which are summed at each value of 2θ to obtain the total intensity used in the middle plot and the main text's Fig. 3. The middle plot shows Gaussian fits to the chi-summed intensity versus 2θ. The bottom plot shows that the relative amplitudes of the Gaussian fits yield the relative population of the A domain $\left(D_A = \frac{I_A}{I_A + I_B} \times 100\%\right)$ versus the measured nominal strain.

Free energy derivation. Here we discuss in more detail the Landau free energy described in the main text:

$$F = \frac{a(T - T^*)}{2}\psi^2 + \frac{b}{4}\psi^4 + \frac{C_{66,0}}{2}\varepsilon^2 - \lambda\psi\varepsilon - h\varepsilon$$

In the high-symmetry (tetragonal) phase, there is no static nematic order ($<\psi>=0$). An applied stress h causes the orthorhombicity to become non-zero, which creates nematic order. Minimizing the free energy first with respect to ψ and then to ε and taking the $\psi = 0$ limit yields the zero-stress nematic susceptibility, $\frac{d\psi}{d\varepsilon} = \frac{\lambda}{a}\left(\frac{1}{T-T^*}\right)$. Taking the resistivity anisotropy $\eta = \frac{\rho_{xx} - \rho_{yy}}{\rho_{xx} + \rho_{yy}}$ to be linearly proportional to the nematic order parameter, $\eta = k\psi$, the elastoresistivity coefficient $2m_{66}$ becomes linearly proportional to the nematic susceptibility, $2m_{66} = \frac{d\eta}{d\varepsilon} = k\frac{d\psi}{d\varepsilon}$. To obtain the renormalized shear modulus C_{66}, we minimize the free energy with respect to ε and then to ψ and use $\frac{dh}{d\psi} = \frac{d\varepsilon}{d\psi}\frac{dh}{d\varepsilon} = \frac{C_{66}}{\left(\frac{d\psi}{dh}\right)}$ to obtain $C_{66} = C_{66,0} - \lambda\frac{d\psi}{d\varepsilon}$.

Below the nematic transition under zero stress ($h = 0$), the nematic order parameter becomes spontaneously non-zero (ψ_S) which drives the spontaneous orthorhombicity (ε_S). Minimizing the free energy with respect to ε yields the magnitude of the orthorhombicity, $\varepsilon_S = \frac{\lambda}{C_{66,0}}\psi_S$. Assuming the spontaneous resistivity anisotropy remains proportional as well ($\eta_S = k\psi_S$), the ratio $\frac{\eta_S}{\varepsilon_S} = \frac{k}{\left(\frac{\lambda}{C_{66,0}}\right)}$ becomes temperature independent and independent of the nematic order parameter. Subbing $\varepsilon = \frac{\lambda}{C_{66,0}}\psi$ into the free energy and minimizing with respect to ψ, we obtain

$$\psi\left(a\left(T - T^* - \frac{\lambda^2}{aC_{66,0}}\right) + b\psi^2\right) = 0$$

As the second term in the outer brackets is always positive (since $b > 0$ is required for stability), we find ψ may have a non-zero value only for $T < T^* + \frac{\lambda^2}{aC_{66,0}} = T_S$, yielding an enhanced nematic transition temperature T_S. The nematic order parameter grows with a mean-field temperature dependence as $\psi_S = \sqrt{\frac{a}{b}(T_S - T)}$, resulting in mean-field temperature dependencies of ε_S and η_S.

Data availability

The data that support the findings of this study are available within the paper and its Supplementary Information. Raw X-ray data are available from the corresponding author upon reasonable request. Source data are provided with this paper.

Acknowledgements

We thank C. Xu, J.-Y. Chen, R. Fernandes, A. V. Andreev and M. Ikeda for discussions. This work was mainly supported by National Science Foundation's Materials Research Science and Engineering Center at the University of Washington (DMR-1719797) and the Air Force Office of Scientific Research under grant FA9550-17-1-0217 and grant FA9550-21-1-0068. J.-H.C. acknowledges the support of the Gordon and Betty Moore Foundation's EPiQS Initiative, grant GBMF6759 to J.-H.C.; the David and Lucile Packard Foundation; the Alfred P. Sloan Foundation; and the Clean Energy Institute funded by the state of Washington. J.L. acknowledges support from the National Science Foundation under grant no. DMR-1848269. This research used resources of the Advanced Photon Source, a US Department of Energy Office of Science User Facility operated for the Department of Energy Office of Science by Argonne National Laboratory under contract no. DE-AC02-06CH11357. J.J.S. was partially supported by the US Department of Energy, Office of Science, Office of Workforce Development for Teachers and Scientists, Office of Science Graduate Student Research programme, administered by the Oak Ridge Institute for Science and Education for the Department of Energy. Oak Ridge Institute for Science and Education is managed by Oak Ridge Associated Universities under contract no. DE-SC0014664.

Author contributions

J.M. grew the samples. J.J.S. and P.M. did the experiments. P.J.R., J.-W.K. and J.L. helped conceive and design the X-ray diffraction measurements at the Advanced Photon Source. J.J.S. analysed the data. J.-H.C. supervised the project. All authors contributed extensively to the interpretation of the data and the writing of the manuscript.

Competing interests

The authors declare no competing interests.

Additional information

Supplementary information The online version contains supplementary material available at https://doi.org/10.1038/s41563-021-01082-4.

Correspondence and requests for materials should be addressed to J.-H.C.

Peer review information *Nature Materials* thanks the anonymous reviewers for their contribution to the peer review of this work.

Reprints and permissions information is available at www.nature.com/reprints.